Key Points:
- The occurrence frequency of Saturn radiation belt transient extensions indicates a possible role for Corotating Integration Regions (CIRs)
- There is high probability (>72%) that transient extensions contribute >10% electron content in the radiation belt
- Preference in outside-in cases independent of local time suggests that electron belts may be largely sustained by convective inflow of transient

Correspondence to:
E. Roussos,
roussos@mps.mpg.de

Sustaining Saturn's Electron Radiation Belts Through Episodic, Global-Scale Relativistic Electron Flux Enhancements

C.-J. Yuan[1,2,3] , **E. Roussos[4]** , **Y. Wei[1,2,3]** , and **N. Krupp[4]**

[1]Key Laboratory of Earth and Planetary Physics, Institute of Geology and Geophysics, Chinese Academy of Sciences, Beijing, China, [2]Innovation Academy for Earth Science, CAS, Beijing, China, [3]Beijing National Observatory of Space Environment, Institute of Geology and Geophysics, Chinese Academy of Sciences, Beijing, China, [4]Max Planck Institute for Solar System Research, Göttingen, Germany

Abstract The L shell distributions of MeV electrons in Saturn's radiation belt are investigated orbit by orbit for the 13-year exploration of Cassini. It is found that in addition to the monotonic decrease profiles, there are orbits showing superimposed transient extensions. The extensions are found to stand out above the background population during 50% of belt crossings. We estimate that there is high probability (>72%) that transient extensions contribute more than 10% electron content in the radiation belt. The high occurrence frequency of one extension every 2–3 weeks, together with the relative content, demonstrate that the extensions constitute a regular and fundamental process populating and sustaining the electron belts of Saturn. The transients regularity excludes interplanetary coronal mass ejections as dominant trigger and implies corotation interaction regions and/or internal processes as candidates. Statistical results suggest that the communication of electrons between the middle magnetosphere and the radiation belts is largely through convective radial transport, which produces transient radiation belt extensions.

Plain Language Summary The electrons with velocities comparable to light speed residing in Saturn's magnetosphere, namely its electron radiation belt, are highly variable. One prominent feature of this variability is that the shape of permanently trapped population can be severely distorted by episodic, global-scale enhancements. A case study suggested that such an enhancement can be rapidly transmitted from large distances to the radiation belts by global-scale flows. These flows act on electrons in a similar manner engine impulses propel a spacecraft on a different orbit around a celestial body. It is of interest the role played by these enhancements on the evolution of the radiation belt, and which dynamic processes are responsible. In this study, enhancements are sought in the radial distributions of radiation belt electrons for the full, 13-year exploration of Cassini spacecraft. It is demonstrated that these enhancements constitute a regular and fundamental process that populates and sustains the radiation belts of Saturn. The enhancements' regularity implies periodic solar wind perturbations and/or internal magnetospheric dynamics as their major triggers. Among the large number of enhancements analyzed, we find evidence for several traveling radially inward, supporting the scenario that electrons are transported from large distances under the influence of global-scale flows.

1. Introduction

At the inner magnetosphere of Saturn, MeV electrons mainly reside in the L shell region from ~2.27 to ~6.7, namely the electron radiation belt (Roussos et al., 2018). The inner boundary ($L = 2.27$) colocates with the outer edge of Saturn's A ring, due to the instantaneous absorption that resulted from high density. The outer boundary at $L \sim 6.7$ is determined as the ≥ 1 MeV omnidirectional integral electron flux drops below ~10^4 cm^{-2} s^{-1} on average (Roussos et al., 2014), which is the typical level for the slot region of Earth's electron radiation belts during quiet times (Vette, 1991). Long-term averaged MeV electron radial profiles present a monotonic decrease toward higher L shells. However, Cassini spacecraft recorded dramatic deviations from this averaged distribution during many of its crossings through the radiation belts (Kollmann et al., 2011; Roussos et al., 2014). At a specific L shell, the MeV electron count rate can vary by 1 order of magnitude between different orbits of Cassini. Significant spatial expansions and shrinkages of the radiation belts were also observed. During a 3-month period in 2011, the outer belt boundary reduced to within $L = 5$

(Roussos et al., 2014), while transient enhancements of MeV electrons in the end of 2016 greatly increased their radial extent (Roussos et al., 2018).

It is therefore of interest which factors shape the radial structure of the radiation belt. The relation between Saturn's electron belts in the inner magnetosphere and ring current located at the middle magnetosphere is well established (Roussos et al., 2014). The ring current provides the seed population for the radiation belt. However, it is not clear if the electron acceleration pathway between the ring current and the radiation belts involves important contributions just from radially inward transport or also from nonadiabatic processes, and if it is continuous or episodic.

Roussos et al. (2018) specifically analyzed several sequential Cassini orbits from 2016. The evolution of a transient extension of MeV electrons was tracked throughout the radiation belts during these orbits. Together with the observations at the middle and outer magnetosphere, the transient extension was attributed to a tail acceleration event that evolved to the inner belts through the ring current. By tracking the perturbation all the way from the magnetotail down to the radiation belt, the authors constrained the radial transport time scale to within 2 to 3 weeks, much faster than expected for slow radial diffusion.

The mechanisms able to cause fast transport and/or acceleration are wave-particle interactions or convection. Shprits et al. (2012) suggest that gyroresonance of electrons with waves may not be efficient in Saturn's magnetosphere, although follow-up investigations (Woodfield et al., 2018, 2019) have put nonadiabatic acceleration back into the spotlight.

It is more straightforward to evaluate the role of convection driven by a global-scale electric field, since its existence has been proved by a number of studies (Andriopoulou et al., 2012, 2014; Paranicas et al., 2005; Roussos et al., 2005, 2007, 2013; Thomsen et al., 2012). Roussos et al. (2018) illustrated that a variable noon-midnight electric field observed at Saturn can trigger fast radial transport. For electrons about 1 MeV, the transport process is especially efficient, since around that energy magnetic drifts cancel out corotation, and the convection electric field can easily bring them inward. Sun et al. (2019) provided convincing evidence to support this corotation-drift resonance (cancelation) scenario by the analysis of electron energy spectra obtained throughout the Cassini mission. Roussos et al. (2018) argued that the variable noon-midnight electric field can explain the fast development and inward transport of the transient electron belt extension observed in 2016. If such transient extensions are frequent, then this electric field could be the prime candidate that links ring current and radiation belts through episodic, adiabatic transport events. However, as that investigation focused on a single event, it remained unclear how common and how significant such transients were for forming and sustaining Saturn's electron belts compared to other mechanisms.

The current research aims to explore the sustainability and capability of transient extensions to contribute to the radiation belt electron content and to search for statistical evidence that are revealing about their origins and dynamics. In section 2, we first introduce the data set utilized in this study and how we processed these data to remove undesired signals from the data. Then in section 3, we present the observations of transient extension events with an electron content index to quantify their contribution to the entire radiation belt and conduct statistical investigations on our event list. Extended discussions and conclusions are given in sections 4 and 5.

2. Data Set and Data Processing

In this survey we use the G1 channel from High Energy Telescope of Low Energy Magnetospheric Measurement System (LEMMS) unit belonging to the Magnetospheric Imaging Instrument (Krimigis et al., 2004). The G1 channel responds primarily to penetrating relativistic electrons and MeV protons that induce significant signals in the radiation belts. Hence G1 is utilized as an omnidirectional integral channel with a threshold at about 1 MeV for electrons (see also Appendix A in Roussos et al., 2011, 2014). The omnidirectional response of G1 reduces the difficulties in data processing which are inevitable for other directional channels due to LEMMS limitations in pitch angle coverage. As long as full pitch angle coverage cannot be obtained, we would be forced to compare only few orbits and times from L shells where pitch angle coverage is similar, which accordingly limits significantly our statistics. In this sense, an omnidirectional channel as G1 is of preference. Further processing is necessary before analyzing G1 data. There are two major factors to be considered: signals contributed by radiation sources other than MeV electrons, and the latitudinal dependence of the count rates.

2.1. Removal of Contributions From Other Radiation Sources

2.1.1. Removal of Signals With Nonmagnetospheric Origin

There are two components contributing to the nonmagnetospheric signals: the gamma rays and neutrons produced by radioisotope generators (RTG) of Cassini, and Galactic Cosmic Rays (GCR). At regions with L shell larger than 15, G1 channel is dominated by RTG and GCR signals, excluding few very short intervals (≤ 1 hr) that high-latitude, quasiperiodic relativistic electron injections were observed by Cassini (Palmaerts et al., 2016; Roussos et al., 2016), strong enough to trigger that channel. Thus, the noise level due to RTG and GCR is retrieved from the G1 measurements at $L \geq 15$. Note that the intensities of GCR decrease as approaching the planet, starting from $L \sim 6$, as shown in Kotova et al. (2019). From a set of orbits late in the mission during 2017, this GCR decrease could be fully resolved and empirically quantified. An average slope of ~ 0.27 count $\cdot \sec^{-1}/R_s$ is used to reduce the measured RTG/GCR rate of every orbit, starting from $L = 6$ and down to $L = 2.27$,

2.1.2. Magnetospheric Proton Contamination Removal

Penetrating >30 MeV protons contribute significantly to G1 signals within the orbit of Enceladus ($L = 3.95$). In order to quantify this contribution we take advantage of measurements near moon L shells, where MeV protons are fully absorbed (Kollmann et al., 2011), and G1 signals are solely from relativistic electrons. Cassini orbits are selected when G1 rates are not dominated by electron signals within Enceladus's L shell, and depletions are present at the moon L shells, as the case shown in Figure 1b. For these selected orbits, we extracted and interpolated data at moon gaps orbit by orbit, in order to obtain a semiempirical radial profile of the electron contribution to the G1 rates. For the aforementioned procedure, we did not use data at the L shell of Tethys (since proton noise in G1 is unresolved there), only the data between $L = 2.27$ and $L = 4$ are used. Then the original G1 data are subtracted by this "pure" electron signal, and what is left is the proton residual.

Note that interpolation is not applied if data are not present. Thus, from each orbit, we can obtain only a portion of the L shell profile of residual proton noise. Inward of $L = 4$ there are three locations that protons are fully depleted: Enceladus ($L = 3.95$), Mimas ($L \sim 3.05$), and Janus and Epimetheus ($L \sim 2.5$). If data stop at $L = 3.5$, then for that orbit we cannot obtain any points constraining the proton noise, because there is no second interpolation point. If data stop at $L = 2.9$, we can only constrain proton noise for that given orbit down to the L shell of Mimas. The first interpolation point will be at $L = 4$, and the second at $L \simeq 3.05$. Obviously, statistics at $L \leq 3$ are worse, so the proton contribution to G1 may have uncertainties. But considering the statistics shown later in Figure 3b, less than 10 transient events are resolved at $L \leq 3$, and all the other transients locate at $L \geq 4$. Thus, the analyses and the conclusions drawn are not influenced by this problem.

Obtaining the residual proton signal is not always possible, because in many cases, the electron contribution in G1 overwhelms the proton one. Figure 1a shows an example of such kind of orbit. We therefore need a way to predict the G1 proton contribution, for cases of which this cannot be directly resolved. For that reason, we have combined the proton residuals from available orbits and linked them to the rates of LEMM-S's MeV proton channel P4. Here we utilize three advantages: (a) the radial profile of the proton belts is nearly identical in all LEMMS MeV proton channels (Kollmann et al., 2013), such that P4 can be considered as representative, (b) the proton belts change marginally with time (Kollmann et al., 2017), such that the correlation of G1 protons with P4 can be assumed valid for all epochs of Cassini and (c) P4 rates have a negligible pitch angle dependence, such that they can be linked with the omnidirectional rates of G1, without any restriction. The P4-scaled G1 proton background is given by:

$$G1(\text{proton}) = 0.95 \cdot 10.0^{1.22213 + 1.01069 \cdot \log(P4(L<4))} \tag{1}$$

Using equation (1), the proton contamination is removed by subtracting its contribution from G1, as in the example shown in Figure 1c.

2.2. Conversion From G1 Count Rates to Omnidirectional Integral Fluxes

We have converted G1 rates to omnidirectional integral fluxes. A first-order empirical conversion of G1 count rates C_{G1} in units of counts$\cdot$s^{-1} into electron fluxes J_{G1} in units of cm^{-2} s^{-1}, using the LEMMS nominal calibration (Armstrong et al., 2009; Krupp et al., 2009) and the empirical method discussed in Appendix B of Roussos et al. (2014) is
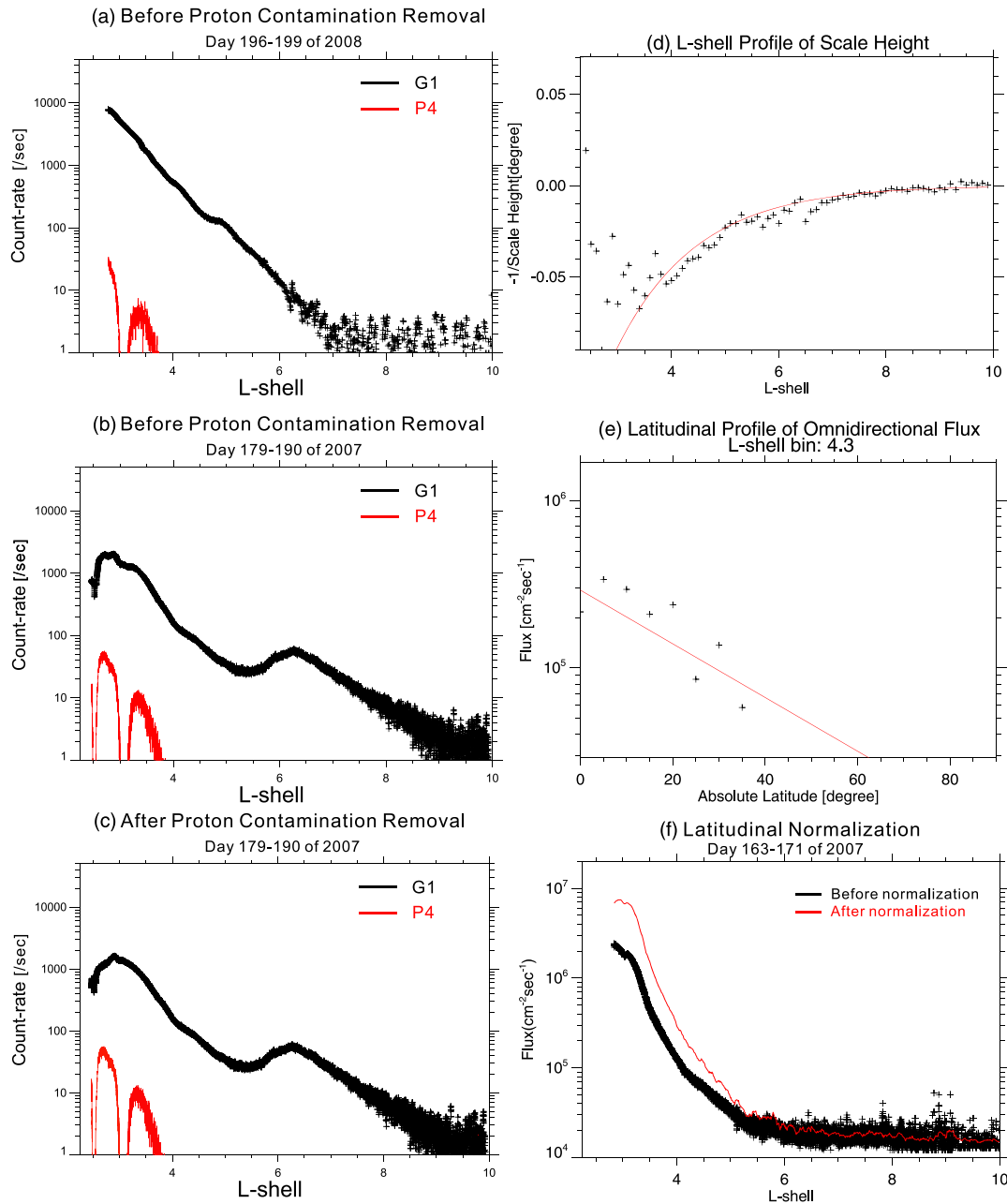
Figure 1. (a–c) Proton contamination removal. (d–f) Latitudinal normalization. (a) Observations from days 196–199 of 2008, before proton contamination removal. The G1 count rate is in black, while in red is the MeV proton count rate from channel P4. MeV electrons overwhelm the signal, so MeV proton contributions to G1 are not visible. (b) Days 179–190 of 2007, before proton contamination removal. Because electron intensities are lower, proton components in G1 become visible (e.g., Mimas moon gap at $L \sim 3$). (c) As in case (b) but after proton contamination removal. At Mimas' orbit, there is no longer moon gap feature, indicating the proton contribution is removed. (d) The L shell distribution of $-\frac{1}{Scale\ Height}$. (e) The distribution of omnidirectional fluxes J_{G1} derived from G1 count rates with latitude at $L = 4.3$. The red line is the fitting result. (f) A latitudinal normalization example. The black line corresponds to the L shell profile before normalization, and the red line is after.

$$J_{G1} = 2,570.4 \cdot 8.511^{\log_{10}(C_{G1})} \tag{2}$$

The G1 rates C_{G1} in this equation is the value after removing the contamination by GCRs, RTGs, and protons, and for values greater than $\sim$5 counts·s^{-1}. It is applicable before conducting the latitudinal correction.

2.3. Latitudinal Normalization

Because the higher latitude Cassini is crossing, the less portion from equatorial pitch angle distribution there is to be sampled, J_{G1} are expected to drop with increasing latitude. This trend has to be removed so that all orbits are comparable, irrespective of Cassini's latitude during the various radiation belt crossings.

We choose to normalize J_{G1} at different latitudes onto the equatorial plane. First, we bin all the data from Cassini's Saturn orbits according to L shell and latitude, and construct a latitudinal profile to which we fit the distribution with a scale height function:

$$J_{G1}(L, \lambda) = J_0(L) \cdot e^{-\frac{\lambda}{H(L)}} \tag{3}$$

$J_{G1}(L, \lambda)$ is the flux at a certain L shell and latitude, $J_0(L)$ means the flux on the magnetic equatorial plane at this L shell, λ is the absolute latitude, and $H(L)$ is the scale height parameter at this L shell. Figure 1d presents the distribution of scale height with L shell. Figure 1e shows an example of the latitudinal profile at $L = 4.3$, from where the scale height at this L shell bin is obtained. Then, for the L shell distribution of each orbit, we normalize $J_{G1}(L, \lambda)$ onto the equatorial plane by using equation (3) of the corresponding L shell bin. An example of the latitudinal normalization is shown in Figure 1f.

The simple scale height function proves to be an adequate description for the purpose of our study, based on Figures 1d to 1f. While there may be natural variations of this scale height with time or for specific belt features (e.g., transient extensions), we believe our approach is relevant, given that in the following paragraphs we focus on large rather than small-scale structures and changes of the belts.

3. Observations

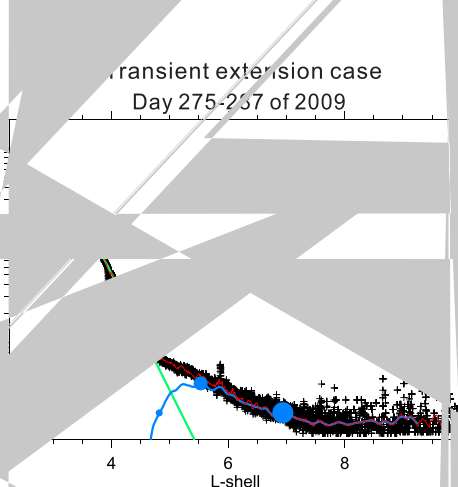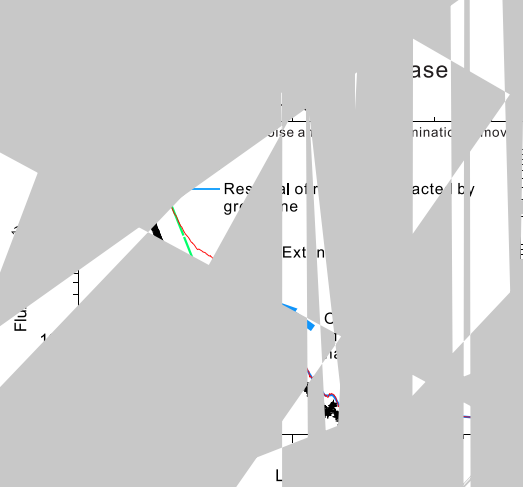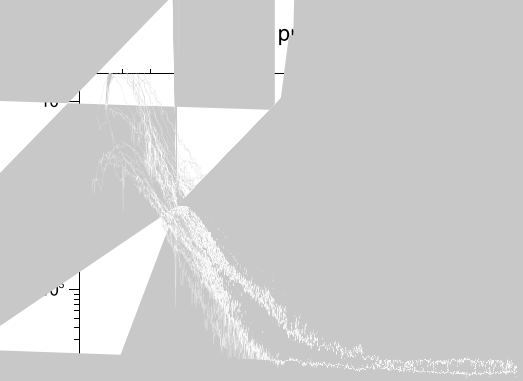### 3.1. Categorization of MeV Electron L Shell Distribution

The averaged L shell distribution from 2005 to 2017 for MeV electron count rates in the radiation belt of Saturn follows a monotonic decrease toward increasing L shell at $L > 2.5$, without abrupt change in radial gradient, as shown in Figure 2a. To determine whether this average distribution is representative, detailed examination orbit by orbit is carried out. The results demonstrate that the radiation belt changes not only in intensity but also in shape. Especially, the L shell distribution may deviate significantly from the average profile; also, the count rate at a certain L shell can vary by an order of magnitude between different orbits, as found in earlier studies. Accordingly, in the following investigations, the L shell distributions of MeV electron count rates from G1 are categorized into two types: average state of radiation belt and perturbed state (with abrupt change in radial gradient).

Typical cases of these two types of distribution are shown in Figures 2b–2d. Figure 2b presents the average-state distribution during an outbound crossing from days 157 to 169 in 2012. Figures 2c and 2d are for two perturbed-state cases. These two cases are characterized by transient extensions with different distribution features. Figure 2c shows the apparent transient extension characteristic of a "bump" distribution in L shell. Whereas in Figure 2d, the transient extension is implicitly presented through a piecewise-slope distribution. The reason for the sharp change in slope at higher L shells is that the extension structure superimposed on the background is not prominent enough to form a "bump" profile.

For both cases shown in Figures 2c and 2d, it is necessary to extract the transient extension from the permanently trapped radiation belt component. This is achieved by making fit to the L shell distribution inward to the extension feature and taking this fit as the permanently trapped distribution not influenced by transient extensions. The beginning and end, or inner and outer boundaries, of L shell interval for making the fit are determined manually for every orbit with transient extension. As shown in Figures 2c and 2d, the green line described by exponential decrease function fits well the L shell profile not influenced by transient extension, at $L \geq \sim 3$. Then we subtract the fit from the total J_{G1} (red line) of both permanent and transient components of radiation belt, and the residual is the extracted extension structure, as presented in Figures 2c and 2d.

3.2. Electron Content Index: Quantification of MeV Electron Distribution

An electron content index is introduced to quantify the overall strength of transient extension structures or the entire radiation belt. We take EC_{TE} to represent the electron content of transient extension, and EC_{RB} to represent the total electron content of radiation belt.

Transient extension case
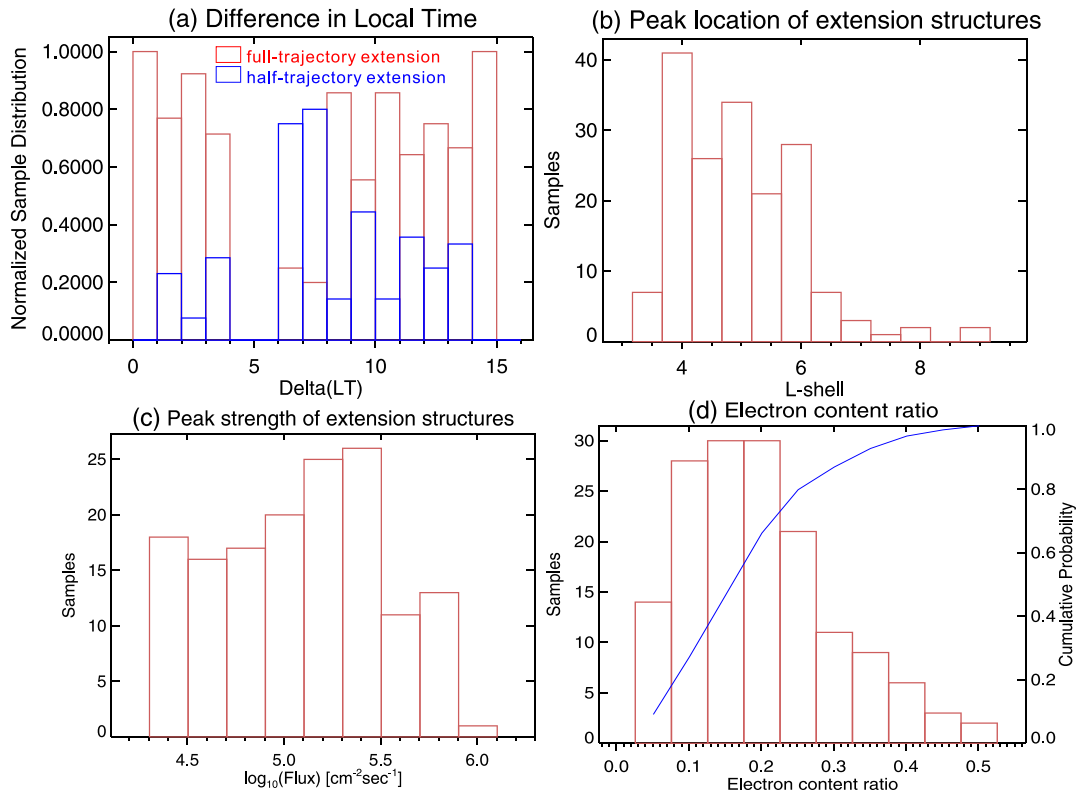Day 275-257 of 2009

L-shell

Figure 3. Histograms of the characteristic parameters for all transient extension events. (a) Normalized histogram of local time (LT) difference of extension peaks between inbound and outbound portions of the same orbit. (b) Histogram of extension peak location in L shell. (c) Histogram of extension peak strength in omnidirectional integral flux. (d) Histogram of the ratio of EC_{TE} to EC_{RB}. A different vertical axis is added to the right side for cumulative probability, shown in blue.

EC_{RB} is the electron content of both permanent and transient distributions (represented by the red line in Figure 2c). EC_{TE} is the electron content of the transient profile only (represented by the blue line in Figure 2c). The upper limit of the integral over L shell is set to be $L = 10$ for both EC_{TE} and EC_{RB}. The lower limit is set to be $L = 3.25$. This value is selected because according to Figure 2a, it can be found from the averaged profile represented by the red line that at regions lower than this altitude, J_{G1} start to drop as it approaches the outer edge of A ring and can no longer be described by a simple exponential function. For the orbits which do not go as deep as $L = 3.25$, we extrapolate the green line (fit of background radiation belt profile) to $L = 3.25$. Thus EC_{RB} from orbits with different periapses can be comparable. There are orbits for which the periapses are very close to the inner edge of the transient extension, so the green line fit cannot be well defined. Such cases are excluded from EC_{TE} calculation.

When calculating the electron content, we should consider the local time (LT) extent of different radiation belt components. For the content of the permanent radiation belt, it is logical to assume that the belt is circumplanetary and its radial profile is representative for all LT to a first order. Transient extensions, on the other hand, are likely limited in LT, and thus the integral has to be multiplied by a factor of $\frac{x}{24}$, where x is the extension's LT width in hours. We provide an estimate of x below.

Figure 3a shows the histogram of local time difference (δLT) between transient belt extensions seen both inbound and outbound of a given orbit ("double-event orbit" for short). Note that the inbound-outbound time differences are generally less than 12 hr, a time scale short enough to consider the transient observed during inbound crossing the same as the one during the outbound counterpart. The geometry of the orbit of Cassini may exert influences on the distribution in this histogram. For instance, a sharp drop in sample number of $\delta LT = 13$ may not indicate that there are fewer transient extensions as wide as 13 hr in LT, but that there are much less orbits covering a 13-hr-wide LT range, and consequently many extension structures spanning such a LT range cannot be captured. To address this limitation, normalization on sample number has been applied to Figure 3a. First, for the orbits during which transient extensions are found

only inbound or outbound ("single-event orbit" for short), we retrieve the L shell and local time of the transient and find the local time at the same L shell during the counterpart crossing. The local-time differences for such orbits are accordingly calculated. Then, for each δLT bin in the histogram, the number of the double-event orbits is divided by the total number of single-event and double-event orbits. The height of red bars shown in Figure 3a corresponds to the normalized sample number of double-event orbits. The blue bars for single-event orbit are overplotted for comparison.

The distributions do not show any clear cutoff or trend that could allow us to unambiguously determine the value of x. The blue bars show that $\delta LT \sim 7$ hr is very common for single-event orbits, but this does not mean that the transient extensions are constrained within 7 hr in width. As can be found from the red bars, the double-event orbits become dominant, as δLT increases from 7 hr. The maximum δLT is 15 hr. Therefore, it is reasonable to take 15 hr as a conservative average estimation of the LT span of transient extensions, even though the high probability to have transient belts with $\delta LT = 15$ implies that they could be even wider. Accordingly, a fraction $\frac{15}{24}$ is applied to EC_{TE}.

Physically, the $\frac{x}{24}$ fraction is determined by two parameters: How wide in longitude was the transient at the time of its formation, and how much time after its formation it has been observed by Cassini. The second parameter controls the importance of drift dispersion on the intensity of the transient. Drift dispersion spreads transient extensions into wider longitudinal ranges. Thus, at a given location the intensity would be reduced. This is the case of transient extensions captured by Cassini using G1 channel. The longer the evolution these belt extensions have experienced due to dispersion, the weaker the signal they generate in G1 intensity. Our empirical solution is to get an average spread of the transient extensions due to dispersion, which is the $\frac{15}{24}$ factor. Then multiply this factor with what is observed along Cassini's orbit, assuming uniformity over a broad local time spread.

Based on the above, an electron content ratio, defined by the ratio of EC_{TE} to EC_{RB}, is introduced to evaluate the relative contribution of the extensions to the radiation belt.

3.3. Statistical Investigations

Our survey includes data from all orbits of Cassini except those from the final phase of the mission (Proximal Orbits). These orbits occur at very high latitudes and show features of mixed electron and proton signals in G1 that proved difficult to process with our method which was tested mostly at low and middle latitudes. Nevertheless, at very high latitudes the G1 signal is a negligible fraction of what is seen in earlier mission phases, such that the results discussed below are not affected by this filtering. We also note that each orbit is separated into its inbound and outbound belt crossings.

Our orbit-by-orbit survey reveals that the extension structures are found during 210 (58%) among 363 inbound/outbound crossings with periapses lower than $L = 6$. Furthermore, there are 183 (50%) crossings during which the transients have a peak signal above 20,000 cm^{-2} s^{-1} (converted from count rates more than a factor 5 over the G1 background noise), which is set to be the criterion on deciding the outer boundary location in Roussos et al. (2014). This criterion is applied to cases with the "bump" feature, as the one shown in Figure 2c, and also to cases presenting "double-slope" feature, as the one shown in Figure 2d. In addition we required that this measurement of peak intensity was part of a coherent, extended population that looks like a transient belt, rather than a stochastic fluctuation of the G1 rates.

The results of our statistical investigations are presented in Figure 3. Transients are resolved as low as $L \sim 3.5$, near the main rings, and up to $L \sim 9$, while their peak intensities are typically centered around $L = 4$–6, as shown in Figure 3b. Figure 3c illustrates that the peak flux of transient extensions can reach as high as 10^6 cm^{-2} s^{-1}, but such events were rare. Note that both the peak flux and EC_{TE} are instrument specific quantities. To provide some context, we have calculated the cumulative probability (p) distribution of content ratio $\frac{EC_{\text{TE}}}{EC_{\text{RB}}}$ to evaluate the contribution of transient extensions to radiation belt. The result is overplotted by blue line in Figure 3d. It can be observed that the probability is low ($p \leq\sim 28\%$) that the content ratio will be less 0.1. In other words, there is high probability ($p >\sim 72\%$) that transient extensions contribute more than 10% electron content in the radiation belt.

We retrieve the difference in L shell of transient extensions from inbound to outbound crossing to examine the radial displacements for a given orbit. Because very small L shell displacements may be due to nonuniform shape of the transient extension across different LT, we only select the cases of which the displacement is $\geq 10\%$ of FWHM of the extension structure. There are 28 "outside-in" events (inward displacement) and
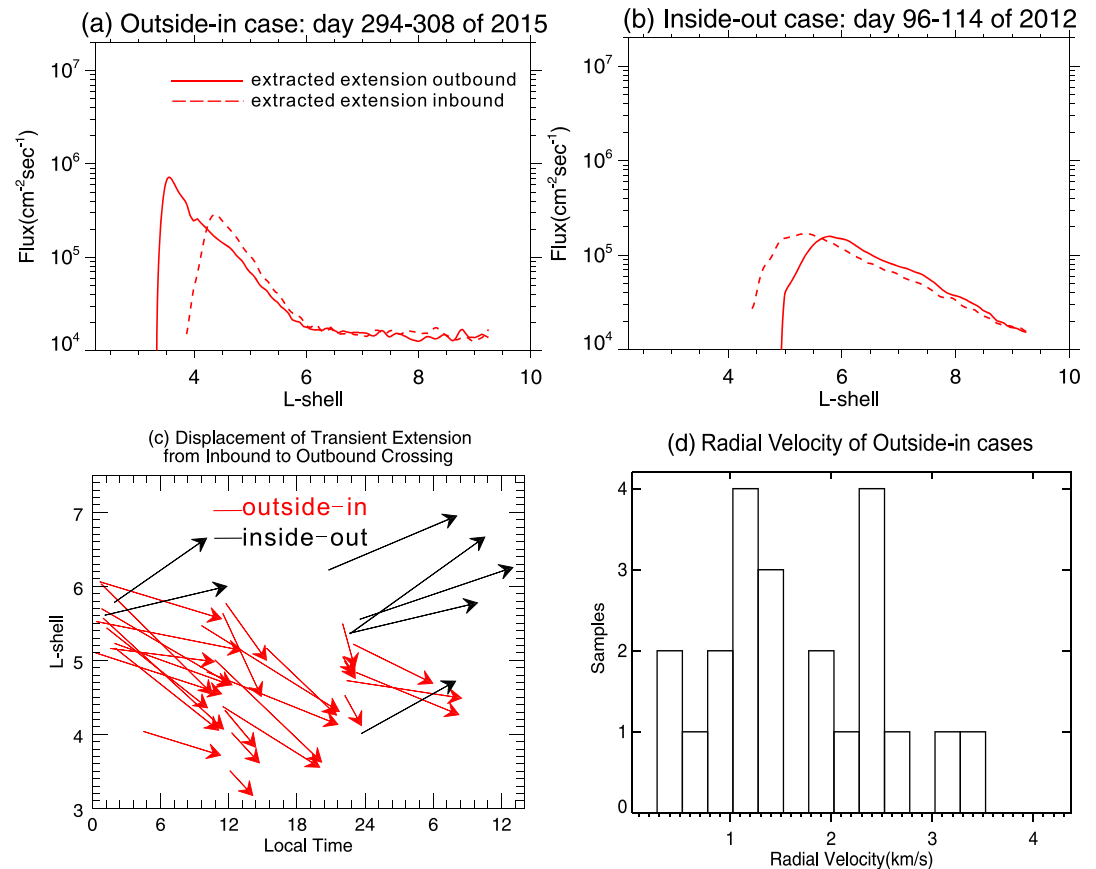
Figure 4. Displacements of transient extensions in L shell and LT. (a) An "outside-in" case during days 294–308 of 2015. The red lines are the L shell distribution of omnidirectional flux of transient extension extracted from the permanently trapped radiation belt components. Dashed linestyle means the data are from inbound crossing, and solid linestyle means the data are from outbound crossing. (b) An "inside-out" case during orbit 96–114 of 2012. (c) The 28 "outside-in" events (red arrows) and 7 "inside-out" events (black arrows) plotted in LT versus L shell coordinates. (d) Histogram of the radial velociy of "outside-in" events.

7 "inside-out" events (outward displacement). In addition, there are 30 events of extensions staying at the same L shell, and 29 events of extensions observed only inbound or outbound. Here we consider one event as a full Cassini orbit with an extension structure. The sum of these event numbers does not match the total of 183 transients given above. The reason is that we have excluded the events for which the extension cannot be separated from the total G1 profile, since a fit of the permanent belt distribution can hardly be determined. Typical "outside-in" and 'inside-out" cases are shown in Figures 4a and 4b, respectively.

Figure 4c shows the LT and L shell displacements of the 28 "outside-in" events (red arrows) and 7 "inside-out" events (black arrows). For all 7 "inside-out" events, the extension moved outward from the nightside to the dayside. However, "outside-in" events occurred either from nightside to dayside (14 out of 28) or from dayside to nightside (5 out of 28). For the remaining 9 "outside-in" events, inbound-outbound LT difference was lower than 3 hr. Further discussions are made in section 4.3, on these "outside-in" and "inside-out" cases.

4. Discussion

In this study we analyzed Cassini relativistic electron data in order to statistically map key properties of electron radiation belt extensions. Our methodology permitted us to resolve weak transient extensions that are otherwise difficult to separate from the nominal radiation belt background and to capture the structure and dynamics of the electron belts in regions with strong proton contamination on the LEMMS signals. It also enabled us to evaluate the contribution of the transient extensions to the entire radiation belt. Our principal findings, for which discussions are focused below, are

(a) Statistical analyses show that transient electron belt extensions occur very frequently.
(b) There is high probability ($p > \sim 72\%$) that transient extensions contribute more than 10% electron content in the radiation belt.
(c) Most transient components that were observed at different L shells between the inbound/outbound portion of the same orbit tend to experience an inward displacement independent of LT. Few events show an outward displacement from the nightside to dayside magnetosphere.

4.1. Occurrence Frequency of Belt Extensions

The large number of the transient extensions indicates that they are caused by dynamic processes that are common for the Saturnian magnetosphere and are efficient in accelerating electrons to MeV energies. Note that the variability of Earth's electron belts is also very significant (e.g., Baker et al., 2019), even though the triggers might be different (Ma et al., 2018; Turner et al., 2019; Yuan & Zong, 2013b, 2013a). Whereas, the proton belts of both planets are relatively less dynamic than their electron counterparts (Kollmann et al., 2017). Earlier studies indicate that several mechanisms may generate transients in Saturn's electron belts. Roussos et al. (2018) show how a very strong shock associated to an Interplanetary Coronal Mass Ejection (ICME) event was behind the appearance of an electron belt transient seen on day 97/2012. They have also linked periodic electron belt expansions to recurring Corotation Interaction Regions (CIRs), while Roussos et al. (2018) discuss how internally driven tail reconnection may also play a role.

With a residence time of Cassini at $3 \leq L \leq 10$ of ~184 days and a total of 183 unique belt extensions identified, we obtain that the rate of observing signatures of transients is about 1 per day. In order to convert this high observation rate into an occurrence rate, we have to consider that a signature of a single transient can be retained for a finite amount of time. Indeed, Roussos et al. (2018) resolved a unique transient for 2–3 weeks. Thus, the effective residence time of Cassini has to be multiplied by that factor, essentially resulting in an occurrence rate of 1 transient every 2–3 weeks. It should be noted that the evolution time scale of the case studied by Roussos et al. (2018) can be obtained due to the reason that it was monitored during the "Ring-Grazing Orbits" with exceptionally short orbital period of 7.2 days. However, most of the Cassini orbits are with much longer periods. As a result, the time scales of the transients are not resolvable for majority of the orbits. So there is little risk that we count one transient for several times. Our estimation on the occurrence frequency, albeit reduced by considering the lifetime of transients, is still high enough and immediately excludes ICME-driven shocks as the extensions' most common trigger. Over the course of the 13-year Cassini mission at Saturn, Roussos et al. (2018) and Roussos et al. (2018) cataloged a total of 48 solar energetic particle (SEP) events that could have originated from ICMEs. Most of them, however, are too weak and unlikely to drive dynamics similar to the observations of day 97/2012. Furthermore, our survey identified many electron belt transients in 2009 and 2010, when no SEP was observed.

Instead, the irregular variability of the electron belts (Roussos et al., 2014) suggests that this occurrence rate is not steady and may become significantly faster or slower. In that respect, CIR compressions, which recur every 2 to 4 weeks over extended periods (Roussos, Jackman, et al., 2018; Roussos, Krupp, et al., 2018) may play a key role in regulating the transient belts' appearance. Also, the fast occurrence rate of belt transients hints that frequent, internally driven reconnection events could act as their trigger (Mitchell et al., 2015; Rymer et al., 2013; Yao et al., 2017).

4.2. Electron Belt Content

A high occurrence rate of belt transients, together with the fact that there is high probability (>72%) that transient extensions contribute more than 10% electron content in the radiation belt, further highlight them as fundamental for sustaining Saturn's electron belts. We may further consider that their content is even greater, as transient belt electrons could remain in the belts for several weeks, as stated in section 4.1. Essentially, the background belt population may be largely composed by old, dispersed transients.

One important aspect we know about electron spectra in the MeV range comes from the study of Sun et al. (2019). They surveyed high-energy resolution electron measurements of LEMMS down to $L = 5$. According to Figure 2c in their work, they found that within about $L = 6$, over 90% of time, the spectra feature a double power law profile, separated at the local corotation-drift-resonance energy (E_{CDR}), that is, the energy at which corotation and magnetic electron drifts cancel out. Recall that according to section 4.1, with a residence time of Cassini at $3 < L < 10$ of ~184 days and a total of 183 unique belt extensions identified, we obtain that the rate of observing signatures of transients is about 1 per day (this is different from the

occurrence rate of transients considering their life time). This very high probability of observing transient extensions, together with the over 90% probability of the occurrence of such E_{CDR} featured spectra, lead to the reasonable assumption that spectra of the belt extensions studied here are also of the double-power law form. This means that they likely contain a large fraction of corotation-drift-resonant (CDR) electrons. CDR electrons at $L < 6$ have energies of 1–3 MeV, the right ones to trigger the G1 channel used here. That explains why the majority of the transients found are located inward of $L = 6$.

4.3. Transport of Transients

A fast transport is hinted by the large number of transients with an inward displacement in the outbound versus inbound orbit segment. Displacements due to a steady-state convection by the noon-midnight electric field would have resulted in a more even distribution of "inside-out" and "outside-in" events between the day and nightside radiation belts compared to what we see. If it was steady convection, the previously circular drift paths (namely at L_0) of the MeV electrons would be shifted in the noon-midnight direction by the noon-midnight electric field. Thus, the displacements relative to L_0 at dayside would be in the opposite direction compared with those at nightside. Then one would expect the distribution of "inside-out" type and "outside-in" type in Figure 4c to be: one type of events majorly locates in the LT range from 0 to 12 hr and from 24 to 12 hr, and the other type resides in the LT range from 12 to 24 hr. As can be easily found in Figure 4c, for outside-in events, there is no such LT preference. Also, the total number of outside-in events is much more than inside-out cases, rather than roughly equal in number. These evidences indicate that at least some of the "outside-in" transients were captured by Cassini while propagating inward due to an ongoing, magnetospheric dynamical process. According to the simulation in Roussos et al. (2018), by imposing a variable noon-midnight large-scale electric field, electrons at E_{CDR} energies can be efficiently transported radially inward. This may also work for the transient extensions. As discussed in section 4.2, it is very possible that the energy spectra of transient extensions are E_{CDR} featured. Large-scale variations in the noon-midnight electric field are known to occur in the dawn-dusk electric field of Jupiter, triggering fast transport of energetic electrons (Han et al., 2018; Murakami et al., 2016). Similar variations at Saturn are hinted by electron belt observations near Saturn's A ring (Roussos et al., 2019).

In addition, we note that the transient extensions are different from other large-scale injections related to interchange instability, which could also occur at $L \leq 10$. The major concern is electron energy. For the interchange injection, the higher the electron energies, the faster the electrons drift longitudinally away from the flux tube previously contains them, before they can be radially transported further inward. Only if the radial speed of the inward flow was very large could it be possible highly energetic electrons being injected further in. The results of test particle simulation shown in Paranicas et al. (2016) provide quantitative evaluations: Suppose that the injection starts at $L = 8$, even if the radial speed of injection flow is as high as 35 km/s, it is only able to transport electrons with energies no higher than 100 keV to $L = 5.9$. In the current study, the G1 channel we use measures integral count rates with a threshold at about 1 MeV. We have estimated the radial speed of the outside-in transient extensions. For each event, we extracted the time difference between the transient observed during inbound crossing and its outbound counterpart. Then together with the displacement in L shell, we calculated the radial speed. The result is presented in Figure 4d. It can be found that the radial speed is at the order of 1–3 km/s. This is a lower limit on the radial speeds, because the transient extension may have reach its outbound observation location before Cassini was there.

5. Conclusions

We conclude that the communication of electrons between the middle magnetosphere and the radiation belts is largely through convective radial transport, which produces transient radiation belt extensions. The occurrence frequency and relative content of these extensions constitute them as one of the dominant transport and acceleration processes of Saturn's radiation belts. Questions remain as to their major trigger, but from the various possibilities available we can safely exclude ICME shocks, while evidences are in favor of CIRs as their candidate trigger. The transients' regularity and fast radial transport, in conjunction with the findings of Sun et al. (2019), indicate that they likely comprise electrons in corotation-drift resonance. Future work on the transients' electron spectra and further analysis of single events and different aspects of our survey results would be necessary to bring closure to new questions opened here.

References

Andriopoulou, M., Roussos, E., Krupp, N., Paranicas, C., Thomsen, M., Krimigis, S., et al. (2012). A noon-to-midnight electric field and nightside dynamics in Saturn's inner magnetosphere, using microsignature observations. *Icarus*, *220*(2), 503–513. https://doi.org/10.1016/j.icarus.2012.05.010

Andriopoulou, M., Roussos, E., Krupp, N., Paranicas, C., Thomsen, M., Krimigis, S., et al. (2014). Spatial and temporal dependence of the convective electric field in Saturn's inner magnetosphere. *Icarus*, *229*, 57–70. https://doi.org/10.1016/j.icarus.2013.10.028

Armstrong, T., Taherion, S., Manweiler, J., Krimigis, S., Paranicas, C., Mitchell, D., & Krupp, N. (2009). Energetic ions trapped in Saturn's inner magnetosphere. *Planetary and Space Science*, *57*(14), 1723–1731. https://doi.org/10.1016/j.pss.2009.03.008

Baker, D. N., Hoxie, V., Zhao, H., Jaynes, A. N., Kanekal, S., Li, X., & Elkington, S. (2019). Multiyear measurements of radiation belt electrons: Acceleration, transport, and loss. *Journal of Geophysical Research: Space Physics*, *124*, 2588–2602. https://doi.org/10.1029/2018JA026259

Baker, D. N., Kanekal, S. G., Blake, J. B., & Pulkkinen, T. I. (2001). The global efficiency of relativistic electron production in the Earth's magnetosphere. *Journal of Geophysical Research*, *106*, 19,169–19,178.

Han, S., Murakami, G., Kita, H., Tsuchiya, F., Tao, C., Misawa, H., et al. (2018). Investigating solar wind-driven electric field influence on long-term dynamics of Jovian synchrotron radiation. *Journal of Geophysical Research: Space Physics*, *123*, 9508–9516. https://doi.org/10.1029/2018JA025849

Kollmann, P., Roussos, E., Kotova, A., Paranicas, C., & Krupp, N. (2017). The evolution of Saturn's radiation belts modulated by changes in radial diffusion. *Nature Astronomy*, *1*(12), 872–877. https://doi.org/10.1038/s41550-017-0287-x

Kollmann, P., Roussos, E., Paranicas, C., Krupp, N., & Haggerty, D. (2013). Processes forming and sustaining Saturn's proton radiation belts. *Icarus*, *222*(1), 323–341. https://doi.org/10.1016/j.icarus.2012.10.033

Kollmann, P., Roussos, E., Paranicas, C., Krupp, N., Jackman, C. M., Kirsch, E., & Glassmeier, K. H. (2011). Energetic particle phase space densities at Saturn: Cassini observations and interpretations. *Journal of Geophysical Research*, *116*, A05222. https://doi.org/10.1029/2010JA016221

Kotova, A., Roussos, E., Kollmann, P., Krupp, N., & Dandouras, I. (2019). Galactic cosmic rays access to the magnetosphere of Saturn. *Journal of Geophysical Research: Space Physics*, *124*, 166–177. https://doi.org/10.1029/2018JA025661

Krimigis, S. M., Mitchell, D. G., Hamilton, D. C., Livi, S., Dandouras, J., Jaskulek, S., et al. (2004). Magnetosphere imaging instrument (MIMI) on the Cassini mission to Saturn/Titan. In T. Russell (Ed.), *The cassini-huygens mission: Orbiter in situ investigations volume 2* (pp. 233–329). Dordrecht, Netherlands: Springer. https://doi.org/10.1007/978-1-4020-2774-1_3

Krupp, N., Roussos, E., Lagg, A., Woch, J., Müller, A., Krimigis, S., et al. (2009). Energetic particles in Saturn's magnetosphere during the Cassini nominal mission (July 2004–July 2008). *Planetary and Space Science*, *57*(14), 1754–1768. https://doi.org/10.1016/j.pss.2009.06.010

Lyons, L. R., & Williams, D. J. (1984). *Quantitative aspects of magnetospheric physics*. Netherlands: Springer. https://doi.org/10.1007/978-94-017-2819-5

Ma, Q., Li, W., Bortnik, J., Thorne, R. M., Chu, X., Ozeke, L. G., et al. (2018). Quantitative evaluation of radial diffusion and local acceleration processes during GEM challenge events. *Journal of Geophysical Research: Space Physics*, *123*, 1938–1952. https://doi.org/10.1002/2017JA025114

Mitchell, D. G., Brandt, P. C., Carbary, J. F., Kurth, W. S., Krimigis, S. M., Paranicas, C., et al. (2015). Injection, interchange, and reconnection. In *Magnetotails in the solar system* (pp. 327–343). Washinton, DC: American Geophysical Union. https://doi.org/10.1002/9781118842324.ch19

Murakami, G., Yoshioka, K., Yamazaki, A., Tsuchiya, F., Kimura, T., Tao, C., et al. (2016). Response of Jupiter's inner magnetosphere to the solar wind derived from extreme ultraviolet monitoring of the Io plasma torus. *Geophysical Research Letters*, *43*, 12,308–12,316. https://doi.org/10.1002/2016GL071675

Palmaerts, B., Roussos, E., Krupp, N., Kurth, W., Mitchell, D., & Yates, J. (2016). Statistical analysis and multi-instrument overview of the quasi-periodic 1-hour pulsations in Saturn's outer magnetosphere. *Icarus*, *271*, 1–18. https://doi.org/10.1016/j.icarus.2016.01.025

Paranicas, C., Mitchell, D. G., Livi, S., Krimigis, S. M., Roussos, E., Krupp, N., et al. (2005). Evidence of Enceladus and Tethys microsignatures. *Geophysical Research Letters*, *32*, L20101. https://doi.org/10.1029/2005GL024072

Paranicas, C., Thomsen, M., Achilleos, N., Andriopoulou, M., Badman, S., Hospodarsky, G., et al. (2016). Effects of radial motion on interchange injections at Saturn. *Icarus*, *264*, 342–351. https://doi.org/10.1016/j.icarus.2015.10.002

Roussos, E., Andriopoulou, M., Krupp, N., Kotova, A., Paranicas, C., Krimigis, S., & Mitchell, D. (2013). Numerical simulation of energetic electron microsignature drifts at Saturn: Methods and applications. *Icarus*, *226*(2), 1595–1611. https://doi.org/10.1016/j.icarus.2013.08.023

Roussos, E., Jackman, C., Thomsen, M., Kurth, W., Badman, S., Paranicas, C., et al. (2018). Solar energetic particles (SEP) and galactic cosmic rays (GCR) as tracers of solar wind conditions near saturn: Event lists and applications. *Icarus*, *300*, 47–71. https://doi.org/10.1016/j.icarus.2017.08.040

Roussos, E., Jones, G. H., Krupp, N., Paranicas, C., Mitchell, D. G., Lagg, A., et al. (2007). Electron microdiffusion in the Saturnian radiation belts: Cassini MIMI/LEMMS observations of energetic electron absorption by the icy moons. *Journal of Geophysical Research*, *112*, A06214. https://doi.org/10.1029/2006JA012027

Roussos, E., Kollmann, P., Krupp, N., Paranicas, C., Dialynas, K., Jones, G. H., et al. (2019). Sources, sinks, and transport of energetic electrons near Saturn's main rings. *Geophysical Research Letters*, *46*, 3590–3598. https://doi.org/10.1029/2018GL078097

Roussos, E., Kollmann, P., Krupp, N., Paranicas, C., Dialynas, K., Sergis, N., et al. (2018). Drift-resonant, relativistic electron acceleration at the outer planets: Insights from the response of Saturn's radiation belts to magnetospheric storms. *Icarus*, *305*, 160–173. https://doi.org/10.1016/j.icarus.2018.01.016

Roussos, E., Krupp, N., Mitchell, D., Paranicas, C., Krimigis, S., Andriopoulou, M., et al. (2016). Quasi-periodic injections of relativistic electrons in Saturn's outer magnetosphere. *Icarus*, *263*, 101–116. https://doi.org/10.1016/j.icarus.2015.04.017

Roussos, E., Krupp, N., Paranicas, C., Carbary, J., Kollmann, P., Krimigis, S., & Mitchell, D. (2014). The variable extension of Saturn's electron radiation belts. *Planetary and Space Science*, *104*, 3–17. https://doi.org/10.1016/j.pss.2014.03.021

Roussos, E., Krupp, N., Paranicas, C. P., Kollmann, P., Mitchell, D. G., Krimigis, S. M., et al. (2011). Long- and short-term variability of Saturn's ionic radiation belts. *Journal of Geophysical Research*, *116*, A02217. https://doi.org/10.1029/2010JA015954

Roussos, E., Krupp, N., Paranicas, C., Kollmann, P., Mitchell, D. G., Krimigis, S. M., et al. (2018). Heliospheric conditions at Saturn during Cassini's ring-grazing and proximal orbits. *Geophysical Research Letters*, *45*, 10,812–10,818. https://doi.org/10.1029/2018GL078093

Roussos, E., Krupp, N., Woch, J., Lagg, A., Jones, G. H., Paranicas, C., et al. (2005). Low energy electron microsignatures at the orbit of Tethys: Cassini MIMI/LEMMS observations. *Geophysical Research Letters*, *32*, L24107. https://doi.org/10.1029/2005GL024084

Rymer, A. M., Mitchell, D. G., Hill, T. W., Kronberg, E. A., Krupp, N., & Jackman, C. M. (2013). Saturn's magnetospheric refresh rate. *Geophysical Research Letters*, *40*, 2479–2483. https://doi.org/10.1002/grl.50530

Shprits, Y. Y., Menietti, J. D., Gu, X., Kim, K. C., & Horne, R. B. (2012). Gyroresonant interactions between the radiation belt electrons and whistler mode chorus waves in the radiation environments of Earth, Jupiter, and Saturn: A comparative study. *Journal of Geophysical Research*, *117*, A11216. https://doi.org/10.1029/2012JA018031

Sun, Y. X., Roussos, E., Krupp, N., Zong, Q. G., Kollmann, P., & Zhou, X. Z. (2019). Spectral signatures of adiabatic electron acceleration at Saturn through corotation drift cancelation. *Geophysical Research Letters*, *46*, 10,240–10,249. https://doi.org/10.1029/2019GL084113

Thomsen, M. F., Roussos, E., Andriopoulou, M., Kollmann, P., Arridge, C. S., Paranicas, C. P., et al. (2012). Saturn's inner magnetospheric convection pattern: Further evidence. *Journal of Geophysical Research*, *117*, A09208. https://doi.org/10.1029/2011JA017482

Turner, D. L., Kilpua, E. K. J., Hietala, H., Claudepierre, S. G., O'Brien, T. P., Fennell, J. F., et al. (2019). The response of Earth's electron radiation belts to geomagnetic storms: Statistics from the Van Allen Probes era including effects from different storm drivers. *Journal of Geophysical Research: Space Physics*, *124*, 1013–1034. https://doi.org/10.1029/2018JA026066

Vette, J. I. (1991). The AE-8 trapped electron model environment (*NSSDC/WDC-A-RS-91-24*). https://doi.org/10.1002/jgra.50251

Woodfield, E. E., Glauert, S. A., Menietti, J. D., Averkamp, T. F., Horne, R. B., & Shprits, Y. Y. (2019). Rapid electron acceleration in low-density regions of Saturn's radiation belt by whistler mode chorus waves. *Geophysical Research Letters*, *46*, 7191–7198. https://doi.org/10.1029/2019GL083071

Woodfield, E. E., Horne, R. B., Glauert, S. A., Menietti, J. D., Shprits, Y. Y., & Kurth, W. S. (2018). Formation of electron radiation belts at Saturn by Z-mode wave acceleration. *Nature Communications*, *9*(1), 5062. https://doi.org/10.1038/s41467-018-07549-4

Yao, Z. H., Coates, A. J., Ray, L. C., Rae, I. J., Grodent, D., Jones, G. H., et al. (2017). Corotating magnetic reconnection site in Saturn's magnetosphere. *The Astrophysical Journal*, *846*(2), L25. https://doi.org/10.3847/2041-8213/aa88af

Yuan, C. J., & Zong, Q. G. (2013a). The double-belt outer radiation belt during CME- and CIR-driven geomagnetic storms. *Journal of Geophysical Research: Space Physics*, *118*, 6291–6301. https://doi.org/10.1002/jgra.50564

Yuan, C. J., & Zong, Q. G. (2013b). Relativistic electron fluxes dropout in the outer radiation belt under different solar wind conditions. *Journal of Geophysical Research: Space Physics*, *118*, 7545–7556. https://doi.org/10.1002/2013JA019066